5th Joint International Symposium on Deformation Monitoring (JISDM), 20-22 June 2022, Valencia, Spain
DOI: http://doi.org/10.4995/JISDM2022.2022.13933

Long and close-range terrestrial photogrammetry for rocky landscape deformation monitoring

Miriam Cabrelles[1], José Luis Lerma[1], Luis García-Asenjo[1], Pascual Garrigues[1], Laura Martínez[2]

[1] Department of Cartographic Engineering, Geodesy and Photogrammetry, Universitat Politècnica de València, Camino de Vera s/n, 46022 Valencia, Spain, (micablo@doctor.upv.es; jllerma@cgf.upv.es; lugarcia@cgf.upv.es; pasgarta@cgf.upv.es)
[2] Department of Roads and Infrastructures, Diputació de València, c/ Hugo de Moncada 9, 46010 Valencia, Spain, (laura.martinez@dival.es)

Key words: *SfM photogrammetry; EDM-based geodetic techniques; 3D modelling; deformation; monitoring; landslides*

ABSTRACT

The paper describes the processing and validation of a series of terrestrial photogrammetric surveys carried out from 2017 to 2020 for monitoring the stability of a cliff in Cortes de Pallás (Spain). The complexity of the target area, which has a strong orography, a water reservoir, and many obstacles such as electrical power lines or vegetation, makes difficult the use of any measurement technique. After considering solutions such as long-range laser scanning or close-range mobile mapping, which were unsatisfactorily tested and therefore rejected for future campaigns, the use of combined short and long terrestrial photogrammetry proved an efficient method for quick and massive monitoring of the entire cliff with an overall accuracy of several centimetres. All the steps undertaken for the centimetre level accuracy deliverables, which include camera calibration, bundle-adjustment, dense point cloud generation, 3D modelling, and validation of the 3D models by using external geodetic information, will be presented. For the sake of conciseness, only results for the last two campaigns (5th and 6th), as well as the comparison between the last (6th) and the first (1st) campaigns, will be discussed. In addition, photogrammetric results will be validated by analyzing the metrics on four target-based micro-geodetic check points, located on key critical areas of the cliff selected by civil and geotechnical engineers from the Department of Roads and Infrastructures.

I. INTRODUCTION

Rockfalls and landslides are common geohazards that can be found in many places all over the world. When they affect sensitive areas with settlements, natural resources, or civil infrastructures like the case at hand in Cortes de Pallás (Spain), government authorities usually demand experts to provide reliable information about the potential risk of those hazards.

Conventional surveying techniques based on global navigation satellite system (GNSS), geodetic instruments like electronic distance meters (EDM), or total stations (TS) can provide accurate coordinates, but they are restricted to only a discrete number of points (Arbanas *et al.*, 2012; Cina and Piras, 2015; Tsai *et al.*, 2012). In the present case, for instance, EDM-based geodetic techniques were applied to establish a ten-pillar high-precision reference frame which was in turn used to determine the coordinates of the check points (ChPs) permanently installed on the cliff with an overall accuracy of 1 mm – 3 mm (García-Asenjo *et al.*, 2019).

On the other hand, image-based sensors and techniques can provide massive information of large areas, although their suitability to rock slope modelling ultimately depends on the quality of ground control, the overall good geometry, and the distance between the sensor and the object (Francioni *et al.*, 2018).

Terrestrial laser scanning (TLS) is also a recurrent and efficient solution for distances shorter than 200 m, but for distances longer than 800 m, the technique becomes expensive and additional problems may arise, *e.g.* inaccurate registration and/or atmospheric refraction (Fan *et al.*, 2015; Harmening and Neuner, 2019; Friedli et al., 2019).

Nowadays, LiDAR mobile mapping systems (MMS) can be an alternative to perform extensive measurement campaigns. Although the attainable accuracy for low-cost solutions when the area has strong limitations is in the range of 3-8 cm, (Di Stefano *et al.*, 2020; Jaboyedoff *et al.*, 2012; Oppikofer *et al.*, 2009) have investigated the usage of light detection and ranging (LiDAR) technology for landslide, rockfall and debris-flow, classifying its applications into four categories: (1) landslide detection and characterisation; (2) hazard assessment and susceptibility mapping; (3) modelling; and (4) monitoring. The authors alerted about the real challenge: to develop new methods to take benefit from high-resolution digital elevation models (HRDEM). Similarly, (Royán *et al.*, 2014) also broadened the concept of forwarding spatial predictions of future failures, understanding pre-failure behaviours of rockfalls, and their implications for implementing early warning systems.

In the present case, the authors tested the possibility of using both static and dynamic LiDAR for long-range mapping, but taking into account the strong site limitations described in Section II A, unsatisfactory results were obtained for two reasons. First, the long-range measurements over 500 m were not detailed enough. Second, the registration over those ranges failed to achieve the high accuracy required for rock cracking patterns characterization.

The usage of digital photogrammetry and unmanned aerial vehicle (UAVs)/drones for landslide mapping and displacement monitoring is also well-known in literature, even for large landslides (Lindner *et al.*, 2016; Rossi *et al.*, 2018). Nevertheless, the use of UAVs in Corte de Pallás was disregarded because the complexity of the area, which includes a hydraulic power plant with many electricity power lines, car traffic, and tourism activities, does not favour the method. Eventually, the combination of close-range and long-range photogrammetry by using different cameras and lenses was deemed to be the optimal solution for mapping and monitoring the complex area of Cortes de Pallás.

This study analyses the attainable performance that can be achieved with the integration of terrestrial photogrammetry (close-range up to 50 m and long-range from 400 m to 800 m) by using well-defined CPs, 3D modelling, and mapping to monitor the area over three years. The results are additionally validated by using four well-defined ChPs whose coordinates were independently determined by making use of precise geodetic techniques. For the sake of conciseness, only 1st, 5th and 6th campaigns are compared and discussed.

The paper is structured as follows: Section II deals with the Materials and Methods; Section III presents the results of three photogrammetric campaigns between 2019 and 2021; Section IV discusses the results from different points of view; and finally Section V draws some conclusions.

II. Materials and Methods

A. *Study site*

The target area is a broad cliff (650 m long, 200 m high and 300 m wide) facing the north side of a flat-topped hill in Cortes de Pallás, Spain (Figures 1 and 2). In 2015, the power plant facilities and several roads skirting the cliff were seriously damaged due to a sudden rockfall. The refurbishment and consolidation work finished at the end of 2017. Then, the Department of Roads and Infrastructures of the *Diputació de València* commissioned the Department of Cartographic Engineering, Geodesy and Photogrammetry, Universitat Politècnica de València (UPV) a three-year project to monitor both the installed anchoring systems as well as the cliff as a whole. The monitoring project includes, among other components, a ten-pillar geodetic network whose stability is periodically monitored by using sub-millimetric EDM techniques (García-Asenjo *et al.*, 2019) along with deformation analysis based on repeatedly measured geodetic networks (Caspary, 1987; Niemeier, 1981). Additionally, the coordinates of the 15 reflectors installed permanently at critical points in the cliff are periodically determined from the pillars with an accuracy of several millimetres by using similar geodetic techniques. As it will be described in Section II B, a subset of those pillars and reflectors was additionally used for the registration and validation of the 3D photogrammetric models.

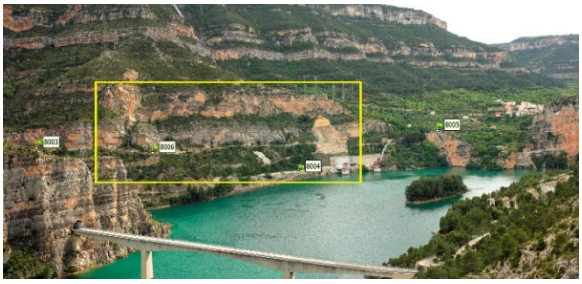

Figure 1. Overall view of the site area. The area to be monitored is displayed in yellow. Location of the 4 CPs used in the 5th and 6th photogrammetric campaigns.

However, the area presents serious limitations for any measurement technique. Aside from the usual problems with obstacles or vegetation, there is a water reservoir that strongly limits the selection of optimal stations for both photogrammetric and geodetic techniques. The stations have to be either very close, thus impeding optimal geometries, or they have to be placed on the opposite shoreline involving distances ranging from 400 m to 1000 m.

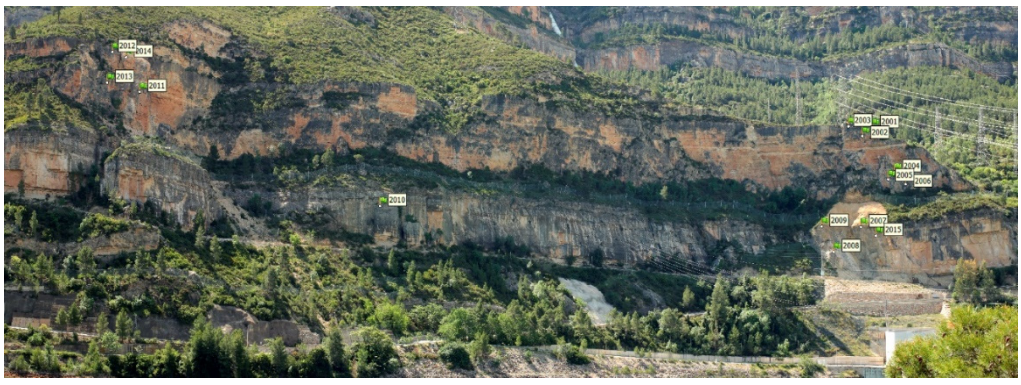

Figure 2. Northside of the hilly area. Location of the 15 ChPs on the slope.

B. *Materials*

Normal and convergent long-range and close-range photogrammetry was used for data acquisition using two digital single-lens reflex (SLR) cameras during the three photogrammetric campaigns: 1) Canon EOS 5D SR (50 MP) with a Carl Zeiss 50 mm lens; and 2) Canon EOS Mark III (21 MP) with a Canon 200 mm lens.

The first camera was used for both close-range and long-range images taken along the roads from both shorelines and from the bridge crossing the reservoir and connecting the shorelines, while the second camera was only used for acquiring the long-range images targeting both the CPs and the ChPs (Figures 1 and 2).

CPs were materialised by big white spheres (∅ 500 mm) temporarily set up on top of the concrete pillars, while ChPs were materialised by small white spheres (∅ 145 mm) which are installed on top of 360º prisms permanently attached to the cliff (Figure 3). The software used for the photogrammetric processing was Agisoft Metashape.

Figure 3. ChPs on the slope.

As ground control for the registration process, there is a significant difference between the first campaign and the subsequent ones. Since the geodetic pillars were not settled yet, the ground control for the first campaign was provided by means of a static GNSS campaign with an overall precision of several centimetres. On the contrary, for subsequent campaigns the ground control was accurately provided by the CPs installed on the pillars of the geodetic reference frame, whose coordinates were determined with an accuracy of several tenths of a millimetre and one millimetre in the horizontal and vertical components, respectively.

C. *Methods*

1) Photogrammetry: Structure-from-motion (SfM) photogrammetry was used to determine the orientation and sparse point cloud for the different campaigns. The cameras were calibrated following self-calibration bundle adjustment using an ideal subset of the images used during the data acquisition. Afterwards, the two calibration reports were used to undertake the bundle adjustment yielding a sparse point cloud. A summary of the photogrammetric data is presented in Table 1.

Table 1. Summary of the 1st, 5th and 6th photogrammetric campaigns

	1st	5th	6th
Date	15/12/17	16/12/20	10/05/21
No. 50 mm images	164	150	166
No. 200 mm images	--	93	137
Avg. GSD [cm]	6.1	3.0	3.0
Avg. distance [m]	515	495	504
No. CPs	5	4	4
No. of ChPs	13	15	15
CPs Error X [cm]	1.5	0.9	0.8
CPs Error Y [cm]	0.9	0.5	0.7
CPs Error Y [cm]	0.7	0.2	0.3
CPs Error XYZ [cm]	1.9	1.0	1.1

For the absolute orientation, the CPs were used to reference the photogrammetric survey to the geodetic survey. Nevertheless, the 15 ChPs were also measured to determine the quality of the photogrammetric survey in each campaign.

The next step tackles the dense point cloud generation, plus cleaning and filtering (Figure 4a and 4c). As the area is extremely large for high resolution 3D modelling, the point cloud was segmented into a mesh of 50 m x 50 m.

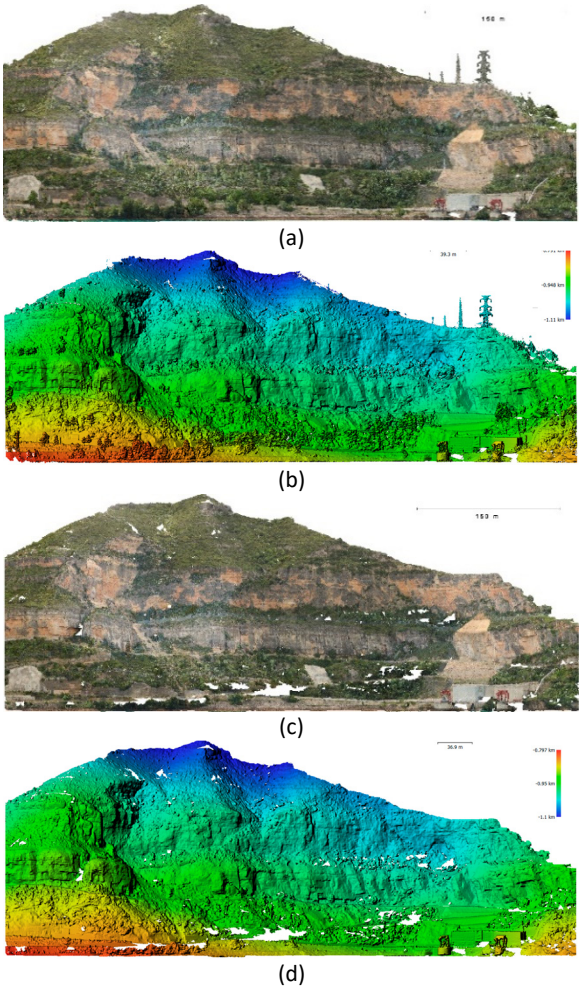

(a) (b) (c) (d)

Figure 4. Generated point cloud and HRDEM for the front hill from the 6th campaign: a) point cloud without filtering; b) HRDSM; c) point cloud filtered; d) HRDEM.

Then, a high-resolution 3D mesh was computed for each meshing patch. It included the 3D meshing refinement, filling small holes and checking/correcting the topology.

Both the digital surface model (DSM) and the digital elevation model (DEM) of the site were also generated at high resolution (HR, Figure 4b and 4d, respectively). Both models can be used to confirm whether the vegetation was properly removed from the hill or not.

The final two image-based steps included texturing and orthoimage creation continued following the conventional SfM photogrammetric pipeline.

This photogrammetric pipeline was repeated for the three campaigns (some numeric values are reported in Table 1). In Section III, the results achieved will be presented.

2) Geodetic measurements: Three EDM-based field campaigns were carried out from 2018 to 2020. For each campaign, around 250 distances were measured using the Kern ME5000 Mekometer (SN 357050). Four original Kern RMO5035 reflectors were used to measure inter-pillar distances (CPs), while distances to reflectors installed permanently in the wall (ChPs) were measured by targeting fifteen Leica 360 reflectors. All the reflectors were calibrated at the UPV calibration baseline (Garcia-Asenjo *et al.*, 2016) in accordance with the full procedure of ISO 17123-4.

The measurement of each distance takes approximately two minutes while the observer measures the meteorological parameters using a traditional Thies Clima Assmann-Type psychrometer (±0.2 K) and a Thommen 3B4.01.1 aneroid barometer (±0.3 hPa). Additionally, all the pillars were equipped with a data-logger Testo 176P1 and a parasol (Figure 5).

Figure 5. Kern ME5000 Mekometer on pillar equipped with a parasol and a data-logger for dry and wet temperatures as well as air pressure.

Prior to the adjustment of each campaign, the following corrections were applied: refraction correction, EDM frequency drift correction and geometric correction. Once these corrections were applied and their corresponding errors computed in order to contribute to the stochastic model, the resulting slope distances were 3D adjusted in two steps. In the first step, only distances between pillars were adjusted to provide a solution for the frame. In the second step, only distances to target points in the wall were adjusted with the pillar coordinates kept fixed.

Finally, as requested by the Diputació de València, all the resulting coordinates and precisions were converted into ETRS89 geodetic coordinates with ellipsoidal height (φ, λ, h), ETRS89-TM30 with orthometric height (E, N, H), and the local system CP2017 (x, y, z), which is the coordinate system used for the photogrammetric process.

After three years no significant displacement was found in the 15 ChPs installed on the cliff, although displacements of several millimetres were detected in some pillars by using congruency tests for deformation analysis (Caspary, 1987; Niemeier, 1981).

Further details about the geodetic measurements and subsequent computations are described in (García-Asenjo *et al.*, 2019; García-Asenjo *et al.*, 2022).

III. Results

The results are presented in two subsections: A) the overall north side of the cliff; B) on the 15 ChPs attached to the wall.

A. *Overall area*

The photogrammetric survey yielded comprehensive results in the form of point clouds (with and without filtering, Figure 4). As stated in Section II, low-resolution and high-resolution 3D models for the different campaigns were computed. Figure 6 displays a picture of a sector determined at high-resolution.

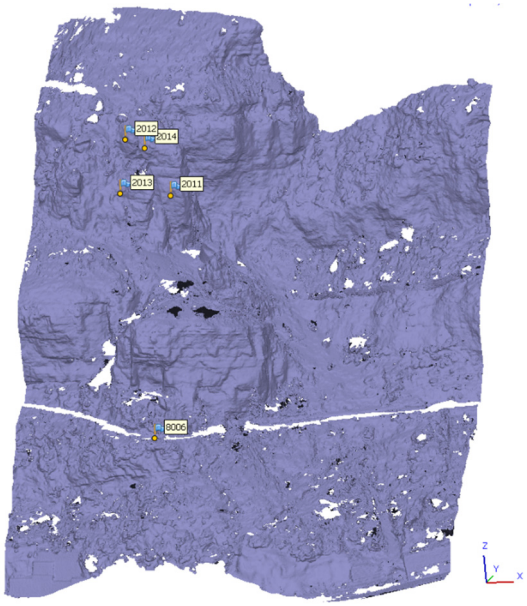

Figure 6. Detail of high-resolution 3D model for the front hill from the 6th photogrammetric campaign.

From them, different geometric comparisons were obtained among campaigns 1-6 (Figure 7a), and 5-6 (Figure 7b), using CloudCompare v. 2.10.2. The quantification of the differences, categorised by ranges, is displayed in Table 2.

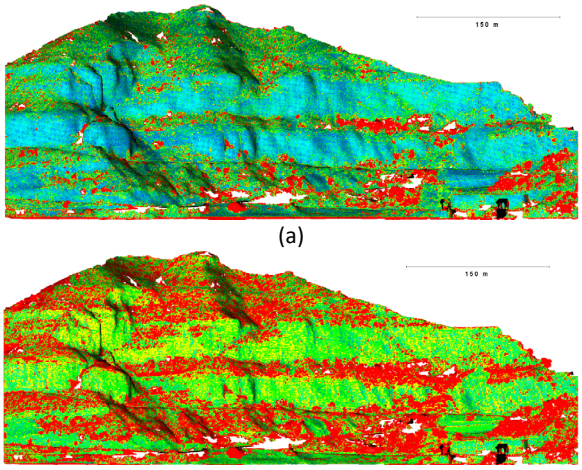

(a)

(b)

Figure 7. Height differences from the 3D models among campaigns: a) 5-6; b) 1-6.

Table 2. Quantitative differences categorised by ranges and photogrammetric campaigns. The first column displays the full colour shading used in Figure 7

Cat.	Distance [cm]	6th-5th (%)	6th-1st [%]
	0-3	12,55	1,77
	3-6	**40,49**	10,37
	6-9	18,00	**16,27**
	9-12	7,91	14,11
	12-15	4,68	9,74
	15-18	3,04	6,84
	18-21	2,11	5,31
	21-24	11,88	**35,59**

From the HRDEM, an orthoimage was created for the 1st photogrammetric campaign.

B. *Check points*

A summary of the metric comparisons on the three campaigns on the left-hand side area targeting four ChPs (Figures 2 and 6) is presented in Tables 3 and 4 for the three campaigns.

Table 3. Coordinates comparison on ChPs between 1st and 6th campaigns

ID	Dx [cm]	Dy [cm]	Dz [cm]	Total [cm]
2011	-0.2	-10.7	-3.9	11.3
2012	2.3	-7.1	-3.4	8.2
2013	-1.0	-10.3	-3.2	10.9
2014	0.2	-9.8	-5.0	11.0

Table 4. Coordinates comparison on ChPs between 5th and 6th campaigns

ID	Dx [cm]	Dy [cm]	Dz [cm]	Total [cm]
2011	1.5	-1.1	-2.4	3.0
2012	1.0	-0.3	-2.1	2.3
2013	1.7	-0.7	-2.2	2.8
2014	1.3	-0.5	-1.7	2.2

Additionally, the differences between the close-range photogrammetry and the EDM coordinates are presented in Tables 5 and 6 for the 5th and 6th photogrammetric campaigns.

Table 5. Coordinates comparison on ChPs between the 5th photogrammetric survey and the geodesy

ID	Dx [cm]	Dy [cm]	Dz [cm]	Total [cm]
2011	-2.7	2.4	-1.8	4.0
2012	-0.4	3.1	-2.1	3.8
2013	2.7	1.8	-1.5	3.6
2014	-2.3	1.3	-1.7	3.1

Table 6. Coordinates comparison on ChPs between the 6th photogrammetric survey and the geodesy

ID	Dx [cm]	Dy [cm]	Dz [cm]	Total [cm]
2011	-0.8	1.4	-3.8	4.1
2012	0.9	2.7	-3.5	4.5
2013	4.6	1.2	-3.9	6.2
2014	-0.9	0.9	-4.2	4.3

IV. Discussion

The bundle adjustment results of the photogrammetric method improved from 1.9 cm (1st campaign) to 1.1 cm (5th and 6th campaigns) (CPs Error XYZ, Table 1). The two main reasons for this improvement can be: first, the inclusion of the 200 mm telelens in the photogrammetric data acquisition; second, the use of the geodetic reference frame as ground control. For campaigns 5th and 6th, the images were only targetting with convergent shots of the white spheres either of the CPs (50 cm in diameter) or the ChPs (14.5 cm in diameter, Figure 3). As it can be seen, substantial improvement was achieved in the Y-axis when comparing the last two photogrammetric campaigns versus the first one.

The centimetric level accuracy (1-2 cm) achieved in the photogrammetric surveys allowed us to determine the height differences among the campaigns, yielding relevant results (Table 2). Most of the differences are in the range of 3-6 cm between the last two campaigns (40,19%, Table 2); 21-24 cm between the 1st and the 6th campaigns (35,59%, Table 2). A plausible explanation for these systematic differences around 25 cm, which are shown in red and form systematic horizontal strips, is that there was substantial vegetation growing from the year 2017 to the year 2020. Therefore, an additional effort in removing vegetation should have been applied. Another significant feature is that there is substantial stability (bluish and greenish colours, Figure 7a) from the last campaigns 5th and 6th, ranging just five months between them.

Taking into account the metric quality of the photogrammetric survey (±2.54 σ), the resulting no significant movement was detected for ChPs 2012 and 2014, while ChPs number 2011 and 2013, show minor vertical displacements (Table 4). On the contrary,

systematic displacements can be seen when the 1st and the 6th campaigns are compared (Table 3). Furthermore, these displacements are only present in both height (Dz) and depth (Dy). Since this systematic shift cannot be reasonably explained by a possible terrain deformation, it should be attributed to deficiencies in the ground control used for the first campaign.

This study confirms that there is no doubt that image-based photogrammetric solutions are an ideal solution for rockfall and landslide monitoring, as suggested for UAVs by (Lindner *et al.*, 2016; Rossi *et al.*, 2018). The terrestrial photogrammetric solutions were always implemented simultaneously with other static long-range terrestrial laser scanners, and one dynamic short-range mobile mapping system (Di Stefano *et al.*, 2020); the latter was not still at the accuracy level of photogrammetry.

V. Conclusions

The multi-image orthogonal and convergent terrestrial photogrammetry acquired with both close-range and long-range visible imagery over a large rocky landscape has demonstrated its capability to achieve centimetre level accuracy. The results from the photogrammetric survey were presented as both graphical and metric reports among the different campaigns.

The integration of 3D photogrammetric models with the external information provided by geodetic techniques is deemed crucial to improve the accuracy of the resulting models so that they can be used for reliable overtime deformation monitoring. Firstly, the ground control of the first campaign, which was based on a single GNSS campaign, has proved to be clearly less accurate than the precise geodetic reference frame periodically monitored. Secondly, the external validation of the photogrammetric 3D models has been only possible because the geodetic techniques provided coordinates for the ChPs with an accuracy one order of magnitude better than those provided by photogrammetry (1 cm – 3 cm).

Metric products such as high-resolution 3D point clouds, low-resolution DEM, HRDEM and orthoimages were deliverables used for deformation monitoring of the large complex and harsh area, not only on the fixed ChPs but also for the entire rough and complex rocky wall.

In the future, the authors would like to integrate SfM photogrammetric solutions with panoramic photogrammetric, taking advantage of the existing geodetic pillars. The idea of integrating mobile mapping solutions, either terrestrial or aerial, is also considered to increase the metric accuracy of the photogrammetric surveys below one centimetre.

VI. Acknowledgements

The authors acknowledge the support of the Department of Roads and Infrastructures, *Diputació de València* to the research and innovation contract 'Control de deformaciones en la ladera norte de la muela de Cortes de Pallás anexa a la carretera CV-428 entre el pk. 14+800 y el pk. 15+950, objeto de las obras de emergencia de sostenimiento y protección (B-267) (T-726)'.

References

Arbanas, Ž., Sassa, K., Marui, H., and Mihalíc, S. (2012). Comprehensive monitoring system on the Grohovo Landslide, Croatia. In *Landslides and Engineered Slopes*: Protecting Society through Improved Understanding (pp. 1441–1447). London: Taylor & Francis Group.

Caspary, W. F. (1987). *Concepts of network and deformation analysis* (School of Surveying, The University of New South Wales, Australia), Monograph 11.

Cina, A., and Piras, M. (2015). Performance of low-cost GNSS receiver for landslides monitoring: test and results. *Geomatics, Natural Hazards and Risk*, 6(5–7), pp. 497–514.

Di Stefano, F., Cabrelles, M., García-Asenjo, L., Lerma, J.L., Malinverni, E.S., Baselga, S., and Pierdicca, R. (2020). Evaluation of long-range mobile mapping system (MMS) and close-range photogrammetry for deformation monitoring. A case study of Cortes de Pallás in Valencia (Spain). *Applied Sciences*, 10(6831), pp. 1–21.

Fan, L., Smethurst, J., Atkinson, P., and Powrie, W. (2015). Error in target-based georeferencing and registration in terrestrial laser scanning. *Computers and Geosciences*, 83, pp. 54-64.

Friedli, E., Presl, R., and Wieser, A. (2019). Influence of atmospheric refraction on terrestrial laser scanning at long range. *Proc. 4th Joint International Symposium on Deformation Monitoring (JISDM)*, 15-17 May 2019, Athens, Greece.

Francioni, M., Salvini, R., Stead, D., and Coggan, J. (2018). Improvements in the integration of remote sensing and rock slope modelling. *Nat. Hazards*, 90, pp. 975-1004.

García-Asenjo, L., Baselga, S., and Garrigues, P (2016). Deformation Monitoring of the Submillimetric UPV Calibration Baseline. *Journal of Applied Geodesy*, 11(2), pp. 107–114.

García-Asenjo, L., Martínez, L., Baselga, S., and Garrigues, P. (2019). Establishment of a multi-purpose 3D geodetic reference frame for deformation monitoring in Cortes de Pallás (Spain). *Proc. 4th Joint International Symposium on Deformation Monitoring (JISDM)*, 15-17 May 2019, Athens, Greece.

García-Asenjo, L., Martínez, L., Baselga, S., Garrigues, P., and Luján, R. (2022). Geodetic monitoring of a high-precision reference frame in Cortes de Pallás (Spain). *5th Joint International Symposium on Deformation Monitoring* (JISDM), 20-22 June 2022, Valencia, Spain.

Harmening, C., and Neuner, H. (2019). Evaluating the performance of a space-and time-continuous deformation model. *Proc. 4th Joint International Symposium on Deformation Monitoring (JISDM)*, 15-17 May 2019, Athens, Greece.

Jaboyedoff, M., Oppikofer, T., Abellán, A., Derron, M.H., Loye, A., Metzger, R., and Pedrazzini, A. (2012). Use of LIDAR in landslide investigations: A review. *Natural Hazards*, 61(1), pp. 5–28.

Lindner, G., Schraml, K., Mansberger, R., and Hübl, J. (2016). UAV monitoring and documentation of a large landslide. *Applied Geomatics*, 8(1), pp. 1–11.

Niemeier, W. (1981). Statistical tests for detecting movements in repeatedly measured geodetic networks. *Developments in Geotectonics*, 16, pp. 335-351.

Oppikofer, T., Jaboyedoff, M., Blikra, L., Derron, M.H., and Metzger, R. (2009). Characterization and monitoring of the Åknes rockslide using terrestrial laser scanning. *Natural Hazards and Earth System Sciences*, 9(3), pp. 1003–1019.

Rossi, G., Tanteri, L., Tofani, V., Vannocci, P., Moretti, S., and Casagli, N. (2018). Multitemporal UAV surveys for landslide mapping and characterization. *Landslides*, 15(5), pp. 1045–1052.

Royán, M.J., Abellán, A., Jaboyedoff, M., Vilaplana, J.M., and Calvet, J. (2014). Spatio-temporal analysis of rockfall pre-failure deformation using Terrestrial LiDAR. *Landslides*, 11(4), pp. 697–709.

Tsai, Z.X., You, G. J.Y., Lee, H.Y., and Chiu, Y.J. (2012). Use of a total station to monitor post-failure sediment yields in landslide sites of the Shihmen reservoir watershed, Taiwan. *Geomorphology*, 139–140, pp. 438–451.